

Layer-dependent evolution of electronic structures and correlations in rhombohedral multilayer graphene

Yue-Ying Zhou^{1,3,†}, Yang Zhang^{1,3,†}, Shihao Zhang^{1,†}, Hao Cai^{1,3,†}, Ling-Hui Tong^{1,3}, Yuan Tian¹, Tongtong Chen⁴, Qiwei Tian¹, Chen Zhang¹, Yiliu Wang¹, Xuming Zou¹, Xingqiang Liu², Yuanyuan Hu², Li Zhang¹, Lijie Zhang¹, Wen-Xiao Wang^{4,*}, Lei Liao², Zhihui Qin^{1,*},
and Long-Jing Yin^{1,3,*}

¹ *Key Laboratory for Micro/Nano Optoelectronic Devices of Ministry of Education & Hunan Provincial Key Laboratory of Low-Dimensional Structural Physics and Devices, School of Physics and Electronics, Hunan University, Changsha 410082, China*

² *College of Semiconductors (College of Integrated Circuits), Hunan University, Changsha, 410082, China*

³ *Research Institute of Hunan University in Chongqing, Chongqing 401120, China*

⁴ *College of Physics and Hebei Advanced Thin Films Laboratory, Hebei Normal University, Shijiazhuang, Hebei 050024, China*

[†]These authors contributed equally to this work.

*Corresponding author: wangwx@hebtu.edu.cn; zhqin@hnu.edu.cn; yinlj@hnu.edu.cn

The recent discovery of superconductivity and magnetism in trilayer rhombohedral graphene (RG) establishes an ideal, untwisted platform to study strong correlation electronic phenomena^{1,2}. However, the correlated effects in multilayer RG have received limited attention, and, particularly, the evolution of the correlations with increasing layer number remains an unresolved question. Here, we show the observation of layer-dependent electronic structures and correlations in RG multilayers from 3 to 9 layers by using scanning tunneling microscopy and spectroscopy. We explicitly determine layer-enhanced low-energy flat bands and interlayer coupling strength. The former directly demonstrates the further flattening of low-energy bands in thicker RG, and the later indicates the presence of varying interlayer interactions in RG multilayers. Moreover, we find significant splitting of the flat bands, ranging from ~50–80 meV, under liquid nitrogen temperature when they are partially filled, indicating the emergence of

interaction-induced strongly correlated states. Particularly, the strength of the correlated states is notably enhanced in thicker RG and reaches its maximum in the six-layer, validating directly theoretical predictions^{3,4} and establishing abundant new candidates for strongly correlated systems. Our results provide valuable insights into the layer dependence of the electronic properties in RG, paving the way for investigating robust and highly accessible correlated phases in simpler systems.

The low-energy flat band constructed in two-dimensional (2D) van der Waals materials has emerged as a new playground for exploring and engineering strongly correlated physics. The most representative family of 2D flat-band systems is twisted moiré heterostructures, in which the moiré superlattices can lead to the emergence of extremely flat minibands that host strong electron–electron interactions⁵. A variety of flat-band-driven exotic quantum phenomena have been consecutively demonstrated in different types of moiré materials, such as twisted bilayer graphene⁶⁻⁹, twisted multilayer graphene¹⁰⁻¹⁷, trilayer graphene/hexagonal boron nitride (hBN) heterostructures¹⁸⁻²¹, and twisted transition metal dichalcogenides^{22,23}. Although extensive studies have been carried out in this rising field, understanding the fundamental physics of the flat-band-induced correlated phases is still precluded. In light of this, expanding the family of 2D flat-band systems and studying the correlated states in even simpler materials are highly desired. Rhombohedral graphene (RG; or *ABC*-stacked graphene) is one such promising flat-band system²⁴⁻³⁰, as it naturally possesses nearly flat bands at the charge neutrality point (CNP), which arise from the unique energy dispersion of $E \sim k^N$ (where N is the layer number)³¹. Unlike moiré heterostructures, RG does not require twisting and thus exhibits higher accessibility and improved structural uniformity. More remarkably, the flat-band electronic correlations in RG are predicted to exhibit a significant dependence on the number of graphene layers^{3,4}. Recently, flat-band-induced superconductivity and magnetism in RG trilayer^{1,2} and correlated states in RG thick-layers³²⁻³⁶ have been discovered, indicating the suitability of RG system for exploring flat-band correlation physics. However, the

flat-band physics in RG multilayers have yet to be sufficiently examined experimentally, and their layer dependence of the electronic structures and correlated effects remains unexplored.

Here we fabricated high-quality RG of 3 to 9 layers and report the observation of layer-dependent electronic structures and correlated states in these systems through scanning tunneling microscopy and spectroscopy (STM and STS) measurements. We observe sharp density of states (DOS) peaks induced by flat bands at the CNP, as well as DOS peaks arising from remote bands in tunneling spectra for all studied $N < 10$ RG. These typical characteristics of RG enable us to accurately examine the layer dependence of the electronic structures. We give direct experimental evidence for layer number-induced extension of flat bands in RG and extract layer-enhanced nearest-neighbor interlayer coupling strength γ_1 , a key parameter that determines the band structures. Furthermore, via measuring filling-varied STS, we observe large splitting of the flat-band peaks at partial fillings with the splitting energy ranging from ~ 50 – 80 meV under liquid nitrogen temperature, indicating the existence of robust interaction-driven correlated states in RG multilayers. In particular, the strength of the observed correlated states exhibits a layer-dependent enhancement and shows a maximum in the 6-layer (6L) RG, directly confirming the theory predictions. We also perform theoretical calculations to interpretate our findings.

Our multilayer RG samples were stacked on hBN layers on SiO₂/Si substrate using van der Waals stacking technique (Methods). The STM/STS measurements were performed at 77 K. Figure 1a shows the schematic of the device scheme in STM measurement and the stacking configuration of RG. For RG multilayers, each layer is *AB*-stacked with the nearest-neighbor and next nearest-neighbor layers, forming an *ABC* stacking order. We fabricated multiple multilayer RG devices including 3L-7L and 9L (see Supplementary Information for details). Figure 1b,c show the large-area STM topographic image and atomic-resolution image of the 6L RG sample, which display relatively flat and impurity-free features. Similar surface topography is observed in all RG samples, indicating the high-quality of our fabricated RG. Besides, there are no large moiré superlattices observed in our RG multilayers, indicating the nonalignment

between the RG and underlying hBN (we intentionally misaligned them during fabrication). The high sample quality and the moiréless feature of the fabricated RG provide an unprecedented platform to investigate the intrinsic electronic properties of RG multilayers.

Figure 1d shows a representative STS curve (i.e., dI/dV - V spectrum reflecting the local DOS of electrons at the measuring point) for the 6L RG. A sharp and pronounced DOS peak (marked by FB) is observed near the Fermi level in the spectrum. This DOS characteristic peak originates from the nearly flat band of RG localized on the top layer, which is similar to what has been extensively observed in trilayer RG^{27,30,37-39}. The flat-band peak and the entire tunneling spectrum exhibit a high degree of homogeneity over a relatively large range (hundreds of nanometers) on the sample surface (see Fig. 1e), demonstrating the ultralow local charge potential fluctuations that also presents the excellent quality of our RG sample. Note that we can still find some regions with varying local doping over micrometer scale, resulting in different fillings of the flat band which can be used to study its correlation effect (see below). Besides the flat-band peak, there exist several minor DOS peaks (marked by \pm RB) at higher energies in the tunneling spectrum of Fig. 1d, which are caused by van Hove singularities located at the remote band edges of RG multilayers. Below we will show that these remote-band peaks can be utilized to determine fundamental parameters of RG band structures.

The high-quality samples with varying layer numbers enable us to access the layer-dependent electronic properties of RG multilayers. Figure 2a shows dI/dV spectra measured in different layer RG. The flat-band peak and remote-band peaks are observed in all studied RG multilayers, which are well replicated by the calculated LDOS (Fig. 2d). We first focus on the flat-band state. The width of the flat-band state ranges from 43–53 meV in our RG (upper panel of Fig. 2b) by measuring the width at half maximum (FWHM) of the DOS peak. These values of the flat-band width are comparable to, and even smaller than that obtained on HOPG—a typical high-quality substrate—under identical experimental conditions (see Supplementary Information for details). This once again demonstrates the exceptional quality of our RG samples. A notable characteristic for the flat-band state is that its DOS peak is stronger in thicker RG. This

feature can be quantitatively evaluated by comparing the relative intensities of the DOS peaks between the flat-band state and the first remote-band states in different layers. As depicted in Fig. 2b (lower panel), the measured relative intensity, I_{FB}/I_{RB} , increases with the RG layers. This behavior can be explained by the further flattening of the bands at the CNP in thicker RG. For RG multilayers, the energy bands at the CNP exhibit a local flatness near the K -point of the Brillouin zone. As the number of layers increases, this flat-band region expands in momentum space, resulting in larger DOS at the CNP for thicker RG (Fig. 2d,e)—which may favor stronger interactions. Although this phenomenon has been well predicted by theoretical models^{4,25}, there is currently no direct experimental confirmation. Our layer-varied spectroscopic measurements thus provide direct experimental evidence about such extension of flat bands in RG multilayers.

We then discuss the higher energy states induced by the remote-band edges. Figure 2c (lower panel) shows the energy separation between positive and negative energy states for the first (red arrows) and second (green arrows) remote-band peaks as a function of layer number. The energy separation decreases with the number of layers, indicating a smaller gap between remote bands and thus providing the enhanced screening effect from these bands in thicker RG. Theoretically, the location of the remote-band states in RG is primarily determined by the number of layers and the nearest-neighbor interlayer coupling strength γ_1 —a key parameter that determines the electronic properties⁴⁰. Therefore, for our layer-definite RG, we can accurately extract the hopping parameter γ_1 through fitting the obtained positions of the remote-band states with the calculated bands (Fig. 2d,e). The obtained γ_1 ranges from 0.36 eV to 0.5 eV (upper panel in Fig. 2c), which is consistent well with recent transport results in trilayer and tetralayer RG^{2,35}, and also comparable to those reported in Bernal-stacked graphene⁴¹. Remarkably, γ_1 exhibits an increase with increasing thickness, indicating an enhanced interlayer interaction in more layers. Theoretically, γ_1 depends exponentially on the interlayer distance of graphene layers—the smaller interlayer distance could result in enhanced γ_1 . We did observe a decreasing trend in the interlayer spacing as the layer number increased through AFM measurements of the

thickness; however, there is a relatively large margin of error in the measurements (see Supplementary Information for details). We attribute the observed variation of the interlayer coupling to the screening effect with a finite screening length in multilayer graphene^{42,43}. Firstly, according to the Thomas-Fermi theory, the screening length is estimated as $\lambda_s = 1/\sqrt{e^2\rho/\epsilon}$ where ρ is DOS. In the RG with more layers, the DOS at the CNP is enhanced (see Fig. 2a,d). Thus, the screening length decreases in thicker RG, leading to the increase of interlayer interactions. Moreover, the substrate easily introduces heavy charge doping in near-substrate graphene layers with a rapidly decayed density (usually within 4-5 layers)⁴². This is evidenced by the larger shift of the flat-band peak away from the Fermi energy observed in our thin samples (Fig. 2a). Consequently, the doped charge could induce a notable additional screening effect in thinner samples, while it only affects several near-substrate layers in thicker samples, further facilitating the enhancement of interlayer interactions in thicker RG.

The observed sharp DOS peaks of the flat-band states in RG multilayers inspire the emergence of electronic correlations when these bands are partially occupied. To examine the correlation effects of flat bands, we conducted filling-varied STS measurements by combining two methods: utilizing local *p-n* junction structures and detecting large regions with varying doping. We first focus on the former case. Nanoscale *p-n* junction structures are easily formed by underlaying charged defects^{44,45} or local intercalation at the interface of van der Waals heterostructures⁴⁶. Figure 3a shows an intercalation-induced subcircular *p-n* junction structure with the size of ~ 20 nm and height of ~ 0.7 nm observed in the 6L RG sample (see Supplementary Information for details). The flat-band peak, which marks the position of the CNP, is located just above and below the Fermi level in the outer and central regions of the *p-n* junction (Fig. 3c), respectively. This explicitly demonstrates the inversion of local doping in the junction (Fig. 3b). With a close examination of the spatially resolved dI/dV spectra measured across the *p-n* junction (Fig. 3c), we can find that the doping exhibits a gradual transition from *p*-type to *n*-type, resulting in a full variation of the flat-band filling. In the *p-n* junction region slightly off its center, the flat-band peak is

partially filled and splits into two peaks with filling-dependent spectral weights (Fig. 3d-f). The peak-to-peak splitting energy of the flat-band state is also varied with the filling states and reaches a maximum of ~ 87 meV at half-filling (see Fig. 3h and Supplementary Information for extraction of the filling factor). Such filling-dependent flat-band peak splitting—with comparable splitting size—and spectral weight redistribution are also observed in other non-intercalation regions, i.e., differently doped flat RG regions with partially filled flat band (see Fig. 3i for the 6L sample). Moreover, the flat-band peak splitting in the p - n junction structure and various doping regions is observed in other RG samples with different layers (see Fig. 4 and Supplementary Information). The above spectroscopic behaviors deviate from the single-particle picture (Fig. 2d,e) and directly demonstrate the emergence of interaction-induced correlated states in RG even under liquid nitrogen temperature, which closely resemble the spectral characteristics of doped flat-band peak in magic angle twisted graphene obtained at lower temperatures⁴⁷⁻⁵⁰.

Next, we investigate the layer dependence of the observed correlated states. Figure 4 shows the layer-dependent dI/dV spectra at nearly half-filling of the flat-band peak (Fig. 4a) and their corresponding splitting energies (Fig. 4b). Note that these data are all measured in the flat regions of RG to avoid any possible extrinsic effects (see Supplementary Information for more data). The correlation-induced spectral splitting of the flat-band peak is evident in all measured 3L–9L RG. Intriguingly, the splitting energies of the flat bands exhibit significantly large values, ranging from ~ 50 meV to ~ 80 meV. The spectral splitting of flat bands has recently been observed in RG system under liquid helium temperature but with much smaller magnitudes. For example, STS study on ABC -stacked 4L region of twisted double-bilayer graphene measured a ~ 10 meV peak-to-peak splitting of the flat bands³³; and the spectroscopic measurement of multilayer RG placed on SiO_2 substrate resulted in a maximum flat-band splitting of ~ 40 meV with a critical temperature of ~ 20 K³². Besides, the transport experiments conducted on RG^{34-36,51-53} also revealed either substantially smaller gaps or lower critical temperatures at the CNP compared to our case. The large correlation-induced splitting of the flat bands observed at liquid nitrogen temperature here directly

demonstrate the existence of strongly electronic interactions in multilayer RG.

The splitting energy of the flat band initially rises and then falls as the RG becomes thicker, reaching its maximum in 6L (Fig. 4b). This behavior indicates a remarkable layer dependence of the correlation effects in RG multilayers. For RG, as the number of layers increases, the flat bands host a larger DOS at the CNP (as demonstrated in Fig. 2), which promotes stronger electronic interactions due to increased electron instability. However, thicker layers also result in greater screening effect on flat-band electrons from the virtual excitations of particle-hole pairs (see Fig. 2), which will weaken the correlations. Consequently, the competition between these two factors will result in a maximum interaction strength at certain critical thickness in RG. Our spectroscopic experiment demonstrates that such critical thickness is six-layer, consistent with recent theoretical predictions^{3,4}. It is worth noting that the splitting energies of the flat bands in 4L–9L RG are all enhanced compared to that in 3L, suggesting stronger correlation effects in these materials. The enhanced flat-band splitting observed in multilayer RG with $3 < N < 10$ therefore establish a series of candidates for investigation of strongly correlated phenomena.

To explore the nature of the observed correlated states as well as verify their layer-dependent behavior, we performed theoretical calculations within a mean-field Hartree-Fock approximation. The calculated Hartree-Fock DOS of the 6L RG are shown in Fig. 3g. A good correspondence with experiments is observed. Our theoretical calculations indicate that the correlated state emerged at the CNP (i.e., nearly half-filling of the flat bands) is a layer antiferromagnetic (LAF) insulating state, and the correlated phases at slightly doped regions (e.g., at the 1/4 or 3/4 filling) flavor spin or valley polarized states (see Methods for details). To further confirm this proposal, we calculated the gap size Δ of the LAF insulating state at the CNP for different layers. The obtained results of Δ for $N < 10$ are shown in Fig. 4c. The calculated LAF gap exhibits a rise-fall variation and shows a maximum at 6L RG, which agrees well with our experimental results in terms of both the dependence on layer and numerical value.

We have examined the evolution of RG band structures and their correlated phases as the number of layers varies through STM/STS measurements. The discovered layer-

dependent flat bands and interlayer hopping strength offer crucial information of the basic band structures of multilayer RG. Especially, we found layer-enhanced correlated states that persist at liquid nitrogen temperature with the maximum interaction strength in 6L. The observations of layer-dependent correlated states in $N < 10$ RG multilayers unveil several intriguing aspects, which can motivate further studies. 1) We clearly determined the layer dependence of the LAF state at the CNP, which had previously exhibited an elusive behavior in RG (3L–5L^{33-36,51,53} and thick layers^{32,52}); 2) The emergence of such evident correlated states at liquid nitrogen temperature is remarkably surprising, albeit potentially influenced by our local measurements. In view of this finding, the multilayer RG represents a promising system that can host highly accessible collective phenomena against thermal fluctuation; 3) Superconductor in RG was only previously discovered in 3L with slight doping¹. Our results demonstrate stronger correlation effects in $3 < N < 10$ RG, accompanied by the manifestation of many-body behaviors in similarly doped regions within the multilayers, thereby presenting a rich and simple material platform that holds immense potential for investigating robust or unconventional superconductivity²⁵.

Methods

Sample fabrications. We fabricated the RG/hBN devices using van der Waals stacking technique. Firstly, we prepared multilayer RG and hBN flakes (42–52 nm thick) on silicon substrates coated with a 285 nm oxide layer through mechanical exfoliation from bulk crystals. The *ABC* domains of RG were identified by Raman spectroscopy. The sample thickness was determined by atomic force microscope. Then we picked up the RG flake using a handle, which is composed of a polyvinyl alcohol (PVA) film and a Polydimethylsiloxane (PDMS) stamp stacked on a glass slide. Subsequently, the RG flake was stacked onto the hBN flake on SiO₂/Si. The hBN flake was annealed at 300 °C for 3 h in a mixture of hydrogen and argon before assembling with RG flake. The graphene layers and hBN layers are intentionally misaligned during the fabrication process to prevent the introduction of large moiré superlattices. The PVA film was removed by dissolution in deionized water. Finally, we made electrical contact to graphene by deposition of 50–70 nm Au (or Cr/Au) electrodes through a mask. The devices were characterized again by Raman spectroscopy to confirm the preservation of *ABC* stacking before being transferred to the STM chamber.

STM/STS measurements. STM/STS measurements were performed in two low-temperature (liquid nitrogen) STM systems (CreaTec) under ultrahigh vacuum ($\sim 10^{-11}$ Torr) and constant-current mode. Similar spectroscopic phenomena of RG were observed in both STM systems, indicating the robustness of our results. The STM topographic images were calibrated against the standard graphene lattice, Si(111)-(7×7) lattice, and Au(111) surface. The STS measurements were measured using a standard lock-in technique (AC bias modulation: 793 Hz and 10–20 mV). The electrochemically etched Pt_{0.8}Ir_{0.2} and W tips were used in the measurements. The sample is located using a long-distance microscope with micron-scale resolution.

Mean-field calculations. The Hamiltonian of RG multilayer including noninteracting section and electron-electron Coulomb interaction is

$$H = \sum_{\mathbf{k}, \alpha, i, j} \psi_{\alpha i}^{\dagger}(\mathbf{k}) h_{ij}^{\tau}(\mathbf{k}) \psi_{\alpha j}(\mathbf{k}) + \frac{1}{2\Omega} \sum_{\mathbf{k}, \mathbf{k}', \mathbf{q}} V_{\mathbf{q}} \psi_{\alpha i}^{\dagger}(\mathbf{k} + \mathbf{q}) \psi_{\beta j}^{\dagger}(\mathbf{k}' - \mathbf{q}) \psi_{\beta j}(\mathbf{k}') \psi_{\alpha i}(\mathbf{k})$$

where $h_{ij}^{\tau}(\mathbf{k})$ is the noninteracting Hamiltonian in the τ valley, and i or j denotes the carbon atom index. And α, β represents the spin or valley index. We adopt the dual-gate screened interaction potential $V_{\mathbf{q}} = \frac{2\pi k_e \tanh(|\mathbf{q}|d)}{\epsilon_r |\mathbf{q}|}$ in our calculations. Here d is set to 50 nm and $k_e = 1.44$ eV nm is the Coulomb constant. To investigate the screening effect, we use the constrained random-phase approximation (cRPA) in the different multilayer graphene systems. The interaction potential becomes $V_{\mathbf{q}}^{cRPA} = \frac{V_{\mathbf{q}}}{1 + \chi V_{\mathbf{q}}}$ where χ is the susceptibility obtained by cRPA calculations. We solve the total Hamiltonian including on-site Hubbard interaction ($U = 5$ eV) by Hartree-Fock approximation with the 96×96 moment grid, and find out the ground interacting state.

The correlated insulating state that occurs at the CNP is a LAF insulating state. Because the flat bands are mainly contributed by the outermost layers, the outermost layers have the largest spin splitting due to electron-electron interactions. Each layer behaves the ferrimagnetism and thus has the non-zero net spin polarization which breaks the time-reversal symmetry. When the Fermi level is tuned away from CNP, e.g., at the 1/4 or 3/4 filling, the ground state is still dominated by correlations, flavoring a spin polarized or valley polarized state (the total energies of the correlated states are lower than those of non-interacting states, e.g., lower by 148~200 μeV per hole or per electron in the 6L RG). But under heavier electron or hole doping, the Fermi level stays far away from flat bands region, the system will transit into the non-interacting paramagnetic phase.

Layer-dependent correlated gap. If only local Hubbard interaction U is taken into consideration, the mean-field solution about the correlated gap Δ is $1 = \frac{U\Omega}{2\pi} \int_0^{\infty} \frac{kdk}{\sqrt{E^2 + \Delta^2/2}}$. Now we use the simplified model of low-energy bands $E = \pm(\hbar v_F k)^N / \gamma_1^{N-1}$. With this approximation, we can obtain that $\Delta^{(N-2)/N} = \frac{U\Omega}{2\pi} \int_0^{\infty} \frac{dx}{\sqrt{1+x^N}} \left(\frac{\gamma_1^{N-1}}{2\hbar^N v_F^N} \right)^{2/N}$ (here Ω is the area of multilayer graphene unitcell). Thus, the

LAF gap Δ of N -layer RG is proportional to $\gamma_1^{2+\frac{2}{N-2}}$. This becomes γ_1^4 in the trilayer graphene ($N=3$), which is consistent with the previous analytical results⁵³. From this formula, we can note that the stronger interlayer hopping γ_1 in the multilayer graphene can lead to the larger gap Δ contributed by the local Hubbard interaction. However, in multilayer graphene with more layers, the influence of the enhanced interlayer hopping γ_1 on the Hubbard-interaction-induced correlated gap becomes weaker.

Enhanced screening effect. We calculate the effective dielectric function under different q in the multilayer graphene with cRPA method. In the rhombohedral trilayer graphene, the dielectric function reaches ~ 16 at the small q , which is close to the previous work⁵⁴. While the number of multilayer graphene is increasing, the screening effect is enhancing remarkably. Especially, the dielectric function can reach the maximum value of ~ 30 in the 6-layer graphene (see Supplementary Information). This strong screening effect can suppress the electron-electron Coulomb interaction, and thus reduce the correlated gap of RG with more layers.

Data availability

The data that support the findings of this work are available from the corresponding authors upon reasonable request.

Acknowledgements

This work was supported by the National Natural Science Foundation of China (Grant Nos. 12174095, 12174096, 62101185, 12204164, 12304217, 11904076 and 51972106), the Natural Science Foundation of Hunan Province, China (Grant No. 2021JJ20026), and the Strategic Priority Research Program of Chinese Academy of Sciences (Grant No. XDB30000000). L.J.Y. also acknowledges support from the Science and Technology Innovation Program of Hunan Province, China (Grant No. 2021RC3037) and the Natural Science Foundation of Chongqing, China (cstc2021jcyj-msxmX0381). The authors acknowledge the financial support from the Fundamental Research Funds

for the Central Universities of China.

Author contributions

Y.Y.Z. and Y.Z. fabricated the samples. Y.Y.Z., Y.Z. and L.H.T. conducted the electrode fabrications and AFM characterizations with the help of Y.T., Y.W., X.Z., X.L., Y.H. and L.L. Y.Y.Z., Y.Z. and L.J.Y. performed the STM experiments and analysed the data. S.Z. performed the mean-field calculations. H.C. performed the tight-binding calculations. W.X.W., Z.Q. and L.J.Y. supervised the experiments. L.J.Y. designed the project. Y.Y.Z., S.Z. and L.J.Y. wrote the manuscript with inputs from all the other authors.

Competing interests

The authors declare no competing interests.

References

1. Zhou, H., Xie, T., Taniguchi, T., Watanabe, K. & Young, A. F. Superconductivity in rhombohedral trilayer graphene. *Nature* **598**, 434-438 (2021).
2. Zhou, H. *et al.* Half- and quarter-metals in rhombohedral trilayer graphene. *Nature* **598**, 429-433 (2021).
3. Muten, J. H., Copeland, A. J. & McCann, E. Exchange interaction, disorder, and stacking faults in rhombohedral graphene multilayers. *Phys. Rev. B* **104**, 035404 (2021).
4. Pamuk, B., Baima, J., Mauri, F. & Calandra, M. Magnetic gap opening in rhombohedral-stacked multilayer graphene from first principles. *Phys. Rev. B* **95**, 075422 (2017).
5. Bistritzer, R. & MacDonald, A. H. Moire bands in twisted double-layer graphene. *Proc. Natl. Acad. Sci. U.S.A.* **108**, 12233-12237 (2011).
6. Cao, Y. *et al.* Unconventional superconductivity in magic-angle graphene superlattices. *Nature* **556**, 43-50 (2018).
7. Cao, Y. *et al.* Correlated insulator behaviour at half-filling in magic-angle graphene superlattices. *Nature* **556**, 80-84 (2018).
8. Sharpe, A. L. *et al.* Emergent ferromagnetism near three-quarters filling in twisted bilayer graphene. *Science* **365**, 605-608 (2019).
9. Lu, X. *et al.* Superconductors, orbital magnets and correlated states in magic-angle bilayer graphene. *Nature* **574**, 653-657 (2019).
10. Cao, Y. *et al.* Tunable correlated states and spin-polarized phases in twisted bilayer-bilayer graphene. *Nature* **583**, 215-220 (2020).
11. Liu, X. *et al.* Tunable spin-polarized correlated states in twisted double bilayer graphene. *Nature* **583**, 221-225 (2020).
12. Park, J. M., Cao, Y., Watanabe, K., Taniguchi, T. & Jarillo-Herrero, P. Tunable strongly coupled superconductivity in magic-angle twisted trilayer graphene. *Nature* **590**, 249-255 (2021).
13. Hao, Z. *et al.* Electric field-tunable superconductivity in alternating-twist magic-angle trilayer graphene. *Science* **371**, 1133-1138. (2021).
14. Polshyn, H. *et al.* Electrical switching of magnetic order in an orbital Chern insulator. *Nature* **588**, 66-70 (2020).
15. Xu, S. *et al.* Tunable van Hove singularities and correlated states in twisted monolayer-bilayer graphene. *Nat. Phys.* **17**, 619-626 (2021).
16. Chen, S. *et al.* Electrically tunable correlated and topological states in twisted monolayer-bilayer graphene. *Nat. Phys.* **16**, 520-525 (2020).
17. Tong, L.-H. *et al.* Spectroscopic Visualization of Flat Bands in Magic-Angle Twisted

- Monolayer-Bilayer Graphene: Coexistence of Localization and Delocalization. *Phys. Rev. Lett.* **128**, 126401 (2022).
18. Chen, G. *et al.* Signatures of tunable superconductivity in a trilayer graphene moiré superlattice. *Nature* **572**, 215–219 (2019).
 19. Chen, G. *et al.* Evidence of a gate-tunable Mott insulator in a trilayer graphene moiré superlattice. *Nat. Phys.* **15**, 237-241 (2019).
 20. Chen, G. *et al.* Tunable correlated Chern insulator and ferromagnetism in a moiré superlattice. *Nature* **579**, 56-61 (2020).
 21. Yang, J. *et al.* Spectroscopy signatures of electron correlations in a trilayer graphene/hBN moiré superlattice. *Science* **375**, 6586 (2022).
 22. Regan, E. C. *et al.* Mott and generalized Wigner crystal states in WSe₂/WS₂ moiré superlattices. *Nature* **579**, 359-363 (2020).
 23. Wang, L. *et al.* Correlated electronic phases in twisted bilayer transition metal dichalcogenides. *Nat. Mater.* **19**, 861-866 (2020).
 24. Olsen, R., van Gelderen, R. & Smith, C. M. Ferromagnetism in ABC-stacked trilayer graphene. *Phys. Rev. B* **87**, 115414 (2013).
 25. Kopnin, N. B., Ijäs, M., Harju, A. & Heikkilä, T. T. High-temperature surface superconductivity in rhombohedral graphite. *Phys. Rev. B* **87**, 140503(R) (2013).
 26. Wang, H., Gao, J.-H. & Zhang, F.-C. Flat band electrons and interactions in rhombohedral trilayer graphene. *Phys. Rev. B* **87**, 155116 (2013).
 27. Xu, R. *et al.* Direct probing of the stacking order and electronic spectrum of rhombohedral trilayer graphene with scanning tunneling microscopy. *Phys. Rev. B* **91**, 035410 (2015).
 28. Pierucci, D. *et al.* Evidence for Flat Bands near the Fermi Level in Epitaxial Rhombohedral Multilayer Graphene. *ACS Nano* **9**, 5432–5439 (2015).
 29. Henck, H. *et al.* Flat electronic bands in long sequences of rhombohedral-stacked graphene. *Phys. Rev. B* **97**, 245421 (2018).
 30. Yin, L.-J. *et al.* High-Magnetic-Field Tunneling Spectra of ABC-Stacked Trilayer Graphene on Graphite. *Phys. Rev. Lett.* **122**, 146802 (2019).
 31. Zhang, F., Sahu, B., Min, H. & MacDonald, A. H. Band structure of ABC-stacked graphene trilayers. *Phys. Rev. B* **82**, 035409 (2010).
 32. Hagymási, I. *et al.* Observation of competing, correlated ground states in the flat band of rhombohedral graphite. *Science Advances* **8**, eabo6879 (2022).
 33. Kerelsky, A. *et al.* Moiréless correlations in ABCA graphene. *Proc. Natl. Acad. Sci. U.S.A.* **118**, e2017366118 (2021).

34. Lee, Y. *et al.* Gate-Tunable Magnetism and Giant Magnetoresistance in Suspended Rhombohedral-Stacked Few-Layer Graphene. *Nano Lett.* **22**, 5094-5099 (2022).
35. Liu, K. *et al.* Spontaneous broken-symmetry insulator and metals in tetralayer rhombohedral graphene. *Nat. Nanotechnol.* <https://doi.org/10.1038/s41565-023-01558-1> (2023).
36. Han, T. *et al.* Correlated insulator and Chern insulators in pentalayer rhombohedral-stacked graphene. *Nat. Nanotechnol.* <https://doi.org/10.1038/s41565-023-01520-1> (2023).
37. Yin, L.-J. *et al.* Observation of chirality transition of quasiparticles at stacking solitons in trilayer graphene. *Phys. Rev. B* **95**, 081402(R) (2017).
38. Yin, L.-J. *et al.* Imaging of nearly flat band induced atomic-scale negative differential conductivity in ABC-stacked trilayer graphene. *Phys. Rev. B* **102**, 241403(R) (2020).
39. Yin, L.-J. *et al.* Imaging Friedel oscillations in rhombohedral trilayer graphene. *Phys. Rev. B* **107**, L041404 (2023).
40. Slizovskiy, S., McCann, E., Koshino, M. & Fal'ko, V. I. Films of rhombohedral graphite as two-dimensional topological semimetals. *Communications Physics* **2**, 164 (2019).
41. McCann, E. & Koshino, M. The electronic properties of bilayer graphene. *Rep. Prog. Phys.* **76**, 056503 (2013).
42. Sun, D. *et al.* Spectroscopic Measurement of Interlayer Screening in Multilayer Epitaxial Graphene. *Phys. Rev. Lett.* **104**, 136802 (2010).
43. Ohta, T. *et al.* Interlayer Interaction and Electronic Screening in Multilayer Graphene Investigated with Angle-Resolved Photoemission Spectroscopy. *Phys. Rev. Lett.* **98**, 206802 (2007).
44. Ghahari, F. *et al.* An on/off Berry phase switch in circular graphene resonators. *Science* **356**, 845-849 (2017).
45. Zhang, J., Jiang, Y.-P., Ma, X.-C. & Xue, Q.-K. Berry-Phase Switch in Electrostatically Confined Topological Surface States. *Phys. Rev. Lett.* **128**, 126402 (2022).
46. Zheng, Q., Zhuang, Y. C., Sun, Q. F. & He, L. Coexistence of electron whispering-gallery modes and atomic collapse states in graphene/WSe₂ heterostructure quantum dots. *Nat. Commun.* **13**, 1597 (2022).
47. Jiang, Y. *et al.* Charge order and broken rotational symmetry in magic-angle twisted bilayer graphene. *Nature* **573**, 91-95 (2019).
48. Kerelsky, A. *et al.* Maximized electron interactions at the magic angle in twisted bilayer graphene. *Nature* **572**, 95-100 (2019).
49. Xie, Y. *et al.* Spectroscopic signatures of many-body correlations in magic-angle twisted

- bilayer graphene. *Nature* **572**, 101-105 (2019).
50. Choi, Y. *et al.* Electronic correlations in twisted bilayer graphene near the magic angle. *Nat. Phys.* **15**, 1174–1180 (2019).
 51. Myhro, K. *et al.* Large tunable intrinsic gap in rhombohedral-stacked tetralayer graphene at half filling. *2D Materials* **5**, 045013 (2018).
 52. Shi, Y. *et al.* Electronic phase separation in multilayer rhombohedral graphite. *Nature* **584**, 210-214 (2020).
 53. Lee, Y. *et al.* Competition between spontaneous symmetry breaking and single-particle gaps in trilayer graphene. *Nat. Commun.* **5**, 5656 (2014).
 54. Huang, C. *et al.* Spin and orbital metallic magnetism in rhombohedral trilayer graphene. *Phys. Rev. B* **107**, L121405 (2023).

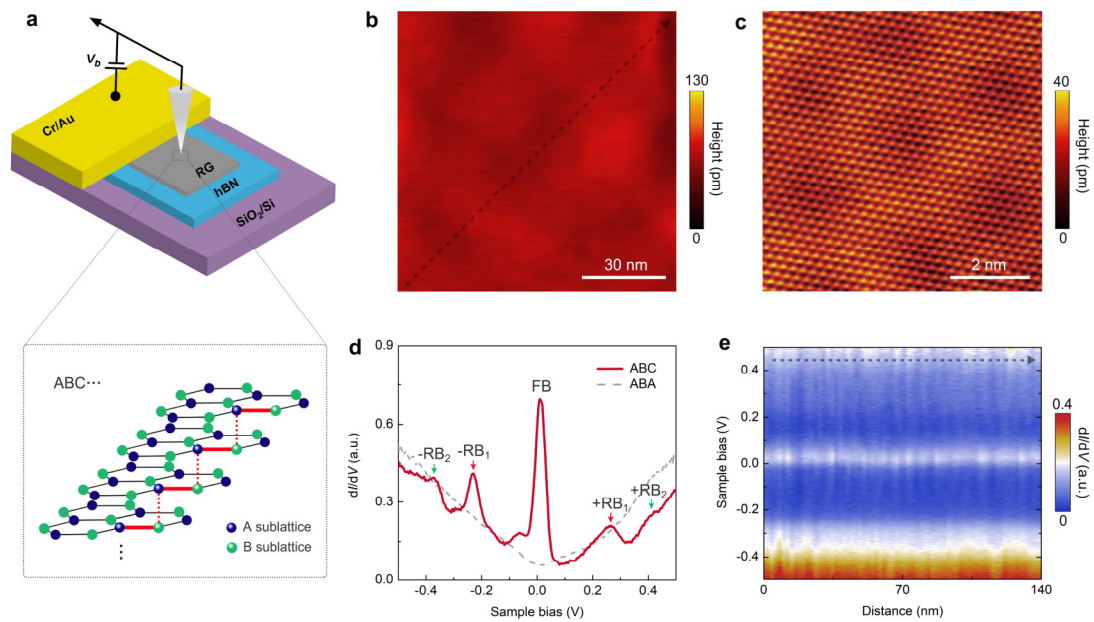


Fig. 1 | Topography and spectroscopy of rhombohedral multilayer graphene. **a**, Schematic of the STM measurement setup and rhombohedral stacking configuration. **b**, An STM topographic image ($100 \text{ nm} \times 100 \text{ nm}$, $V_b = -0.6 \text{ V}$, $I = 0.1 \text{ nA}$) of a 6L RG. **c**, An atomic-resolution STM image ($7 \text{ nm} \times 7 \text{ nm}$, $V_b = -0.6 \text{ V}$, $I = 0.1 \text{ nA}$) of the 6L RG showing extremely weak moiré superlattices with a small period of approximately 2.7 nm formed between the RG and hBN. **d**, Typical tunnelling conductance (dI/dV) spectroscopy of the rhombohedral (*ABC*) and *ABA* 6L graphene measured in the same device. FB: flat band; +RB₁ (-RB₁): the first remote conduction (valence) band; +RB₂ (-RB₂): the second remote conduction (valence) band. **e**, Contour plot of spatially resolved dI/dV spectra measured along the arrow in the topographic image **b**.

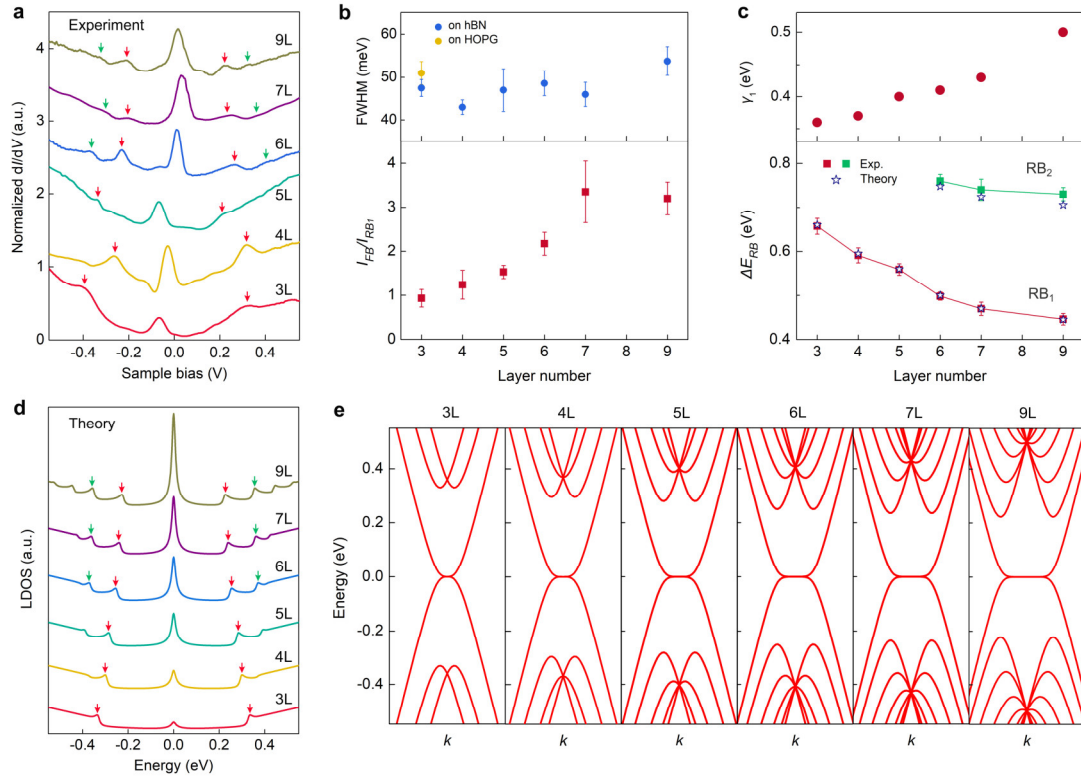


Fig. 2 | Band structure evolution of rhombohedral multilayer graphene. **a**, dI/dV spectra of 3L–7L and 9L RG. Arrows mark the positions of remote band peaks. Curves are vertically shifted for clarity. **b**, Upper panel: Width of the flat-band peak as a function of layer number. Blue and orange dots represent data for RG on hBN and HOPG, respectively. Lower panel: Relative intensity of the DOS peaks between the flat-band state (I_{FB}) and the first remote-band states (I_{RB1}) in different layers. **c**, Upper panel: Obtained nearest-neighbor interlayer coupling strength γ_1 in different layers by fitting. Lower panel: Energy separation of the first (red squares) and second (green squares) remote bands as a function of layer number. The hollow stars are theoretically fitting results to the experimental data. Error bars in **b** and **c** represent the standard deviations of the data. **d**, Calculated noninteracting LDOS on the top layer of 3L–7L and 9L RG. **e**, Single-particle band structures of 3L–7L and 9L RG obtained by the simplest tight-binding model with the nearest-neighbor intralayer coupling $\gamma_0 = 3.16$ eV.

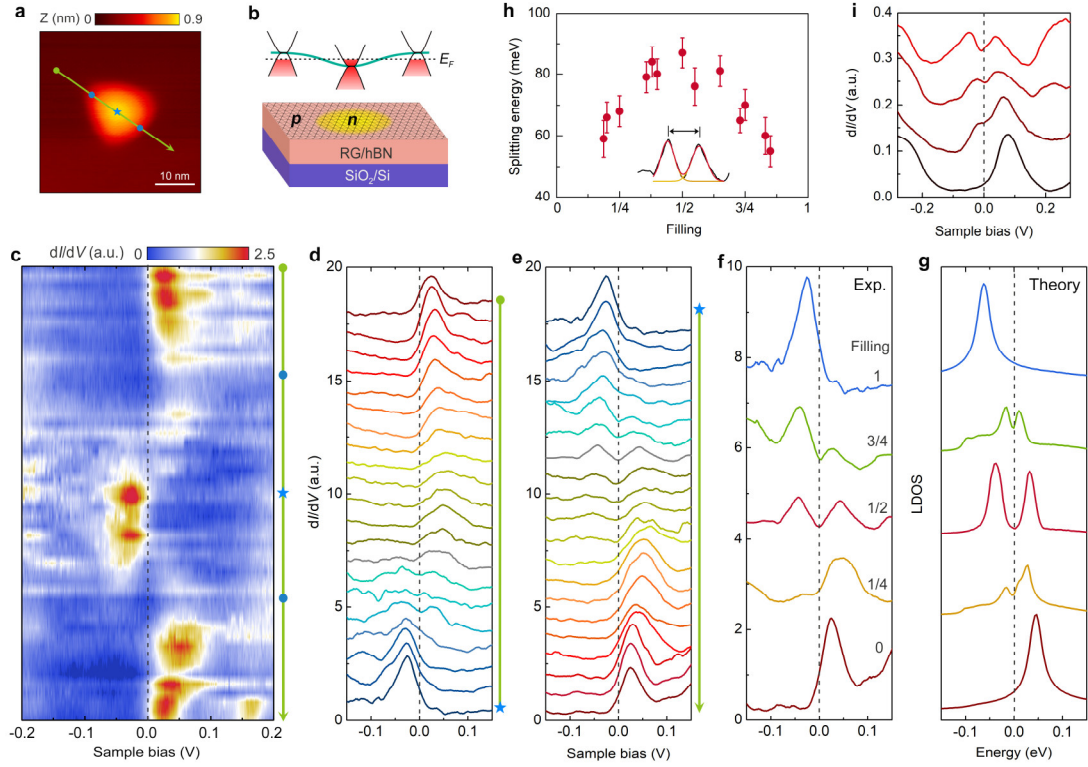


Fig. 3 | Electronic correlations in rhombohedral 6-layer graphene. **a,b,** The STM topographic image (**a**, $40 \text{ nm} \times 40 \text{ nm}$, $V_b = -0.6 \text{ V}$, $I = 0.1 \text{ nA}$) and schematic (**b**) of a *p-n* junction structure on the surface of 6L RG. **c,** Contour plot of spatially resolved STS spectra acquired along the arrow in the topographic image **a**. The blue dots and star denote the boundaries and center of the *p-n* junction, respectively. **d,e,** Spatially resolved dI/dV spectra taken from outside to the center of the *p-n* junction (**d**) and from the center to outside of the *p-n* junction (**e**) extracted from **c**. **f,** Representative dI/dV spectra with different filling states of the flat-band peak measured at the *p-n* junction region. **g,** Calculated LDOS on the top layer of 6L RG under different fillings corresponding to **f**. **h,** Splitting energy of the flat-band peak as a function of filling extracted from **c**. The inset shows an example of the splitting energy extraction. Error bars were estimated by combining the fitting uncertainty and standard deviation of the data. **i,** Representative tunneling spectra of 6L RG recorded at flat regions with varying doping. The flat-band peak exhibits clear splitting at partial fillings. The curves are shifted vertically for clarity.

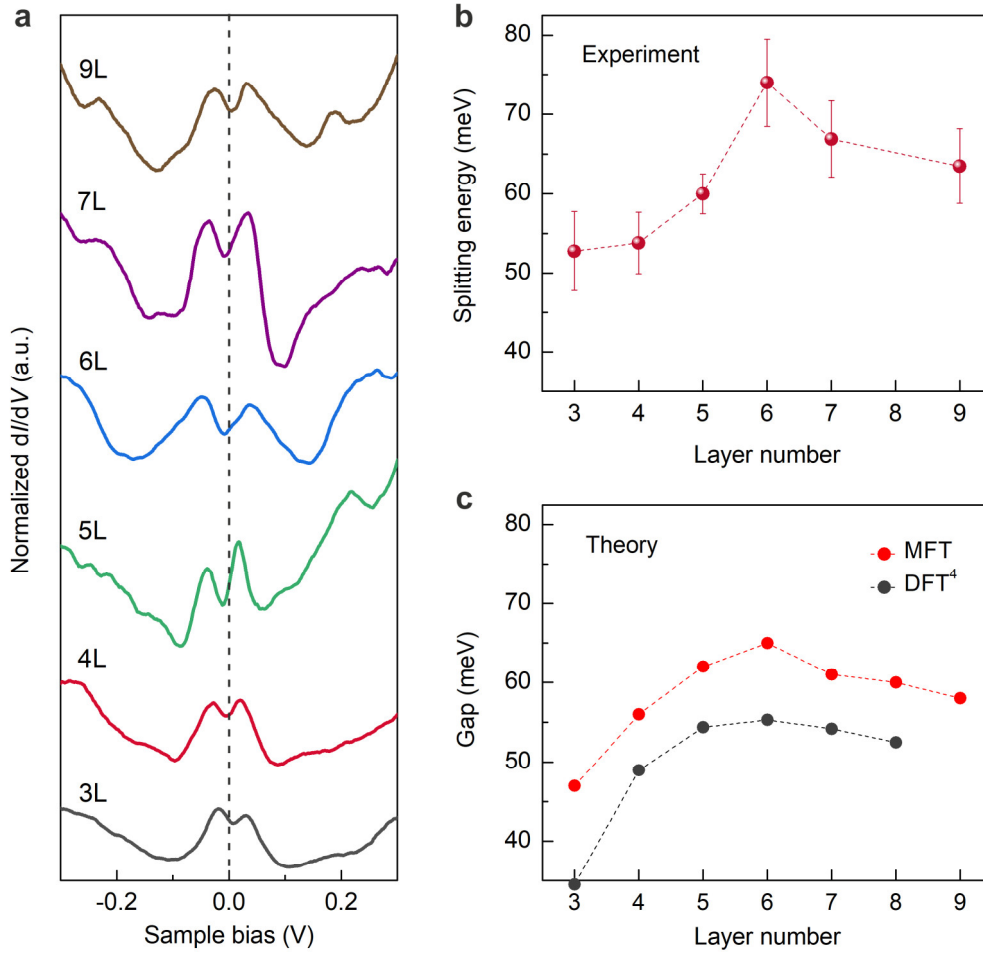


Fig. 4 | Layer dependence of electronic correlations. **a**, Representative STS spectra of 3L–7L and 9L RG for nearly half filling of the flat-band peak at 77 K. The tunneling spectra are taken at flat regions of the samples. The curves are shifted vertically for clarity. **b**, Splitting energy of the flat-band peak (half filling) as a function of layer number. Error bars represent the standard deviations of the data. **c**, Theoretical energy gap of the correlated state at half filling under 77 K. The red circles are our mean-field theory (MFT) results. The black circles indicate density functional theory (DFT) results extracted from literature⁴.